A strong Atlantic Meridional Mode event in 2009: The role of mixed layer dynamics

Gregory R. Foltz[1], Michael J. McPhaden[2], and Rick Lumpkin[1]

[1]NOAA/Atlantic Oceanographic and Meteorological Laboratories, Miami, FL

[2]NOAA/Pacific Marine Environmental Laboratory, Seattle, WA

Corresponding author: gregory.foltz@noaa.gov

9 March 2011

Abstract

In the first half of 2009, intense anomalous cooling of sea surface temperatures (SSTs) in the equatorial North Atlantic (ENA; 2°N–12°N) triggered a strong Atlantic meridional mode event. During its peak in April–May, SSTs in the ENA were 1°C colder than normal and SSTs in the equatorial South Atlantic (5°S–0°) were 0.5°C warmer than normal. Associated with the SST gradient were anomalous northerly winds, an anomalous southward shift of the intertropical convergence zone, and severe flooding in Northeast Brazil. This study uses in situ and satellite observations to examine the mechanisms responsible for the anomalous cooling in the ENA during boreal winter and spring of 2009. It is found that the cooling was initiated by stronger than normal trade winds during Jan–Feb 2009 associated with an anomalous strengthening of the atmospheric high pressure system in the subtropical Atlantic. Between 6°N–12°N, unusually strong trade winds cooled the ocean through wind-induced evaporation and deepened the mixed layer anomalously by 5–20 m. Closer to the equator, surface equatorial winds responded to the anomalous interhemispheric SST gradient, becoming northwesterly between the equator and 6°N. The anomalous winds drove upwelling of 0.5–1 m day^{-1} during March–April, a period when there is normally weak downwelling. The associated entrainment heat flux at the base of the mixed layer led to unusually cool SSTs in the central basin, further strengthening the anomalous interhemispheric SST gradient. These results emphasize the importance of mixed layer dynamics in the evolution of the meridional mode event of 2009 and the potential for positive coupled feedbacks between wind-induced upwelling and SST in the equatorial North Atlantic.

1 Introduction

Interannual to decadal variability in the tropical Atlantic is influenced by the Atlantic meridional mode (AMM), characterized by an anomalous meridional gradient of sea surface temperature (SST) between the tropical North and South Atlantic (Nobre and Shukla 1996). Anomalously warm SSTs in the tropical North Atlantic relative to the South are associated with anomalous southerly surface winds and a northward anomalous displacement of the intertropical convergence zone (ITCZ). Conversely, anomalously cold SSTs in the North Atlantic relative to the South are associated with anomalous northerly winds and a southward shift of the ITCZ. The AMM exerts a strong influence on rainfall in Northeast Brazil and the Sahel, since rainfall in these regions is closely linked to the seasonal movement of the ITCZ (Lamb 1978; Hastenrath and Greischar 1993; Giannini et al. 2003). The AMM tends to peak in boreal spring, when SST variability in the tropical North Atlantic is strongest and the ITCZ is most sensitive to the meridional gradient of SST (Xie and Carton 2004, Hu and Huang 2006).

An important step toward understanding the coupled variability of the AMM is to understand what drives SST variability associated with this mode. Interannual variability of SST in the tropical Atlantic is strongest in the northeastern basin (15°W-40°W, 2°N-20°N) and in the eastern equatorial Atlantic, in connection with the AMM and Atlantic Niños, respectively (Huang et al. 2004). SST variability in the tropical North Atlantic (TNA; 12°N–25°N) is driven primarily by changes in wind-induced latent heat loss (Carton et al. 1996). The surface wind variability itself is influenced by the North Atlantic Oscillation (NAO) and atmospheric teleconnections from the eastern equatorial Pacific (Enfield and Mayer 1996, Czaja et al. 2002). Changes in shortwave radiation from low-level cloudiness and African dust appear to play an

important secondary role (Tanimoto and Xie 2002, Foltz and McPhaden 2008). In contrast, relatively little is known about what drives SST variability in the equatorial North Atlantic (ENA; 2°N–12°N), which underlies the mean position of the ITCZ. This is a region with climatologically warm SSTs (27°C, averaged during MAM between 10°W–50°W, 2°N–12°N) and where SST anomalies are therefore likely to have a significant influence on atmospheric circulation and rainfall, and hence the AMM. Modeling studies suggest that ocean dynamics play an important role in this region (Carton and Huang 1994, Carton et al. 1996). However, there is very little direct observational evidence to support this, and it is unclear which oceanic processes are important.

In 2009 there was a strong negative AMM event that was intiated by anomalous cooling in the TNA. The cold SST anomalies during January–February 2009 coincided with a moderate La Niña in the equatorial Pacific, stronger than normal convection in the Amazon, and an anomalously strong Atlantic subtropical high pressure system, all of which are consistent with enhanced trade winds and cooler than normal SSTs in the TNA. The coldest SST anomalies shifted southward to the ENA during Feb–Mar 2009. The AMM peaked shortly thereafter in March–May, when surface winds in the tropical Atlantic are most sensitive to the cross-equatorial gradient of SST and positive wind-evaporation-SST feedback is strongest (Xie and Carton 2004). By one measure, the anomalous meridional SST gradient in the boreal spring of 2009 was the strongest since satellite SST measurements began in 1982 (Foltz and McPhaden 2010a; Fig. 1). The SST gradient and its associated surface wind anomalies drove a southward displacement of the ITCZ, contributing to severe flooding in Northeast Brazil (Fig. 1b,c). The surface wind anomalies forced equatorial Rossby waves, which reflected from the

4

western boundary and caused abrupt anomalous cooling of the equatorial cold tongue in the summer of 2009 (Foltz and McPhaden 2010a). Cold SST anomalies in the TNA persisted into the boreal summer of 2009, conspiring with a developing Pacific El Niño to produce below-normal tropical cyclone activity (nine tropical cyclones developed in the Atlantic during 2009, the fewest since 1997). The low activity in 2009 is consistent with previous analyses which show that the Atlantic hurricane season is influenced by the state of the equatorial Pacific and SSTs in the TNA (Wang et al. 2006; Latif et al. 2007).

In the past several years there have been substantial improvements to the long-term observational network in the tropical Atlantic Ocean. The global array of Argo floats reached completion in the mid 2000's (Gould et al. 2004), and four Prediction and Research moored Array in the Tropical Atlantic (PIRATA) buoys were deployed as part of the Northeast Extension in 2006–07 (Bourlès et al. 2008). In this study we use these relatively new measurements, together with ongoing satellite observations, to analyze the causes of the anomalous cooling in the North Atlantic (2°N–25°N) in 2009. This region is chosen because of the strong anomalies here that were well sampled by in situ observations (Fig. 2). In comparison, SST anomalies in the South Atlantic were weaker, and in situ observations were sparser.

The rest of the paper is organized as follows. We first describe the data sets used. The evolution of the SST anomalies is then presented in relation to surface wind and subsurface ocean anomalies. The mixed layer temperature balance is analyzed using Argo and satellite data and compared to results from two PIRATA moorings. Finally, the results are summarized and discussed.

2 Data

A combination of satellite, in situ, and atmospheric reanalysis data sets is used to examine the evolution of anomalous conditions in the tropical Atlantic during 2009 and to analyze the mixed layer temperature budget.

2.1 Satellite data, reanalysis fields, and Argo

The satellite data sets consist of SST, surface winds, and outgoing longwave radiation (OLR). SST is available from the Tropical Rainfall Measuring Mission (TRMM) Microwave Imager (TMI) and the Advanced Microwave Scanning Radiometer for EOS (AMSR-E). These data are blended together using optimal interpolation and are available as daily averages on a $0.25° \times 0.25°$ grid from June 2002 to the present from Remote Sensing Systems (ftp.discover-earth.org/sst). We have regridded these data to a $1° \times 1°$ resolution. Surface wind velocity from the SeaWinds instrument on the Quick Scatterometer (QuikSCAT) satellite is available from Institut Français de Recherche pour l'exploitation de la Mer (IFREMER)/Centre ERS d'Archivage et de Traitement (CERSAT) on a $0.5° \times 0.5° \times$ daily grid from July 1999 to November 2009 (ftp://ftp.ifremer.fr/ifremer/cersat/products/gridded/mwf-quikscat). Wind stress is calculated using a constant drag coefficient of 1.5×10^{-3} and an air density of 1.29 kg m^{-3}. The NOAA interpolated OLR, available on a $2.5° \times 2.5°$ grid for 1979–present, is used to detect regions of atmospheric deep convection (Liebmann and Smith 1996).

Horizontal currents averaged in the upper 30 m are available from the Ocean Surface Current Analysis-Realtime (OSCAR, Bonjean and Lagerloef 2002). This product uses satellite sea level, wind stress, and SST, together with a diagnostic model, to calculate velocity on a $1° \times 1°$ grid every five days for the period 1993–present.

6

We also use combined satellite/in situ data sets of SST and precipitation. Monthly optimally interpolated SST is available on a 1°×1° grid from December 1981 to the present (Reynolds et al. 2002; podaac.jpl.nasa.gov/sea_surface_temperature/reynolds/ oisst/). The Global Precipitation Climatology Project (GPCP) provides monthly mean precipitation from January 1979 to the present on a 2.5°×2.5° grid (Adler et al. 2003; http://www.cdc.noaa.gov/cdc/data.gpcp.html). These data sets are used to put the 2009 anomalies into perspective with the longer-term variability in the tropical Atlantic (Fig. 1). We also use daily surface atmospheric pressure, air temperature, and specific humidity from the NCEP/NCAR reanalysis for the time period 1982–2009 on a 2°×2° grid (Kalnay et al. 1996). The surface pressure data are used to calculate atmospheric indices during 2008–09 (Table 1). The air temperature and specific humidity data are used with QuikSCAT wind speed and TMI/AMSR-E SST to calculate surface latent and sensible heat loss. Surface shortwave radiation and net longwave emission are obtained from the TropFlux analysis on a 1° × 1°× daily grid for 1989–2009 (Kumar et al. 2011). This product calculates surface shortwave radiation by combining a satellite-based product (Zhang et al. 2004) with satellite outgoing longwave radiation. Net surface longwave radiation in TropFlux is calculated from the ECMWF reanalysis after bias and amplitude correction.

Monthly averaged mixed layer depth, thermocline depth, and the temperature 10 m below the mixed layer are computed using temperature and salinity profiles from Argo floats during 2005–2009, when the coverage in the tropical Atlantic is highest. The vertical resolution of the temperature and salinity profiles is 5 to 10 m. We use profiles which have their shallowest measurement at a depth of 10 m or less. There are 3465 profiles fitting this criterion in the equatorial North Atlantic region that we focus

on in this study (2°N–12°N, 15°W–45°W).

For all data sets except Argo, anomalies are calculated with respect to the daily mean seasonal cycle computed using data from 2003–2008, when all products are available. Anomalies of Argo-based quantities are calculated based on the 2005–2008 monthly mean seasonal cycle. Because of the exceptional strength of the negative AMM event in 2009, our results are not sensitive to the time period used to calculate the seasonal cycles.

2.2 PIRATA

Measurements from two PIRATA moorings complement the satellite and reanalysis products. The moorings are located at 4°N, 23°W and 12°N, 23°W (Fig. 2c). Both moorings measure subsurface temperature, salinity, and velocity, as well as air temperature, relative humidity, wind velocity, rainfall, and shortwave radiation. The mooring at 12°N, 23°W additionally measures downward longwave radiation and barometric pressure. Because of significant gaps in the buoy 10 m velocity records, these data are used only for validation of OSCAR currents and are not used directly in the temperature budget analyses.

Subsurface temperature at 12°N, 23°W is measured at depths of 1, 5, 10, and 13 m, and with 20 m spacing between 20 m and 140 m. Measurements are made at the same depths at the 4°N, 23°W mooring except that data at 5 m are not available. Salinity is available from both moorings at depths of 1, 10, 20, 40, 60, and 120 m. In addition, the mooring at 12°N measures salinity at 5 m and 80 m. Missing data in the temperature records are filled with vertical linear interpolation. At 12°N, 23°W temperature is missing at depths of 13 m and 20 m during 2008. At 4°N, 23°W temperature is missing at 10 m in 2007. Gaps in the salinity records occur at 5 m and

20 m during 2008 at the 12°N location and at 10 m during 2007 at the 4°N mooring.

3 Results

In this section we examine the processes responsible for generating the SST anomalies in the tropical North Atlantic during 2009. A description of the surface conditions is presented first, followed by an analysis of the mixed layer temperature budget.

3.1 Evolution of the 2009 anomalies

The SST anomalies in 2009 developed over a span of several months and were strongest between 10°S–25°N (Fig. 2). In January 2009 there was an anomalous intensification of the northeasterly trade winds in the tropical North Atlantic (TNA; 12°N–25°N; Fig. 2a). Surface wind speed anomalies during January peaked at $\sim$2 m s^{-1} in the 15°N–20°N band, decreasing to 0.5–1 m s^{-1} just north of the equator. Cold SST anomalies were strongest in the northeastern basin, reaching a maximum of 1–1.5°C off the coast of Northwest Africa (Fig. 2a). To the south of the strongest anomalous cooling, a band of weaker negative SST anomalies developed between the equator and 5°N. This band of anomalously cold SSTs was associated with anomalous northerly winds between 20°W–40°W centered near $\sim$2°N (Fig. 2a). The sign of the meridional wind and SST gradient anomalies in this region is consistent with forcing of the northerly wind anomalies by the southward anomalous SST gradient (e. g., Lindzen and Nigam 1987).

By March 2009 the anomalously strong trade winds had relaxed in the TNA, with anomalously low wind speed between 10°N–20°N (Fig. 2b). The strongest negative SST anomalies in March were located farther south, between the equator and 15°N, increasing in magnitude northeastward from the coast of Brazil to a maximum of 3°C off the coast of Northwest Africa. Anomalous northerly winds on the southern edge of

9

the band of coldest SST anomalies (5°S–2°N) intensified between January and March (Fig. 2a,b).

Between March and May the region of strongest cold SST anomalies off the coast of Northwest Africa weakened slightly and shifted southwestward (Fig. 2c). Northerly surface wind anomalies between 5°S–2°N strengthened further, especially in the western basin. SSTs became anomaloulsy warm between 5°S–2°N, peaking at >1°C between 10°W–20°W. The warm SST anomalies in the equatorial South Atlantic were much shorter-lived than the cold anomalies to the north, however. By July the warm anomalies on the equator were replaced by cold anomalies of up to 2°C (Fig. 2d). Foltz and McPhaden (2010a) showed that the strong equatorial cooling was caused by western boundary-reflected upwelling Kelvin waves. Between May and July SSTs became anomalously warm to the north of 15°N, and the cold SST anomalies between the equator and 15°N weakened considerably. Surface winds returned to normal throughout most of the basin.

The initial trigger for the strong meridional mode event in 2009 can be traced to the anomalous intensification of the TNA trade winds in January and February. The enhanced trade winds are consistent with La Niña conditions in the eastern equatorial Pacific during the winter of 2008–09 and a positive North Atlantic Oscillation (NAO) index in January 2009 (Table 1). The anomalously strong trade winds in January and February 2009 cannot be explained entirely by ENSO and the NAO, however: The 2008 La Niña in the Pacific was stronger than the La Niña in 2009, and the NAO index was of the same sign and comparable in magnitude between the years (Table 1). Based on the NAO and ENSO indices for 2008 and 2009, therefore, wind speed in the TNA during these years should have been similar. Instead, winds were slightly weaker

than normal in Jan–Feb 2008, but two standard deviations stronger than normal in Jan–Feb 2009 (Table 1).

The stronger winds in 2009 relative to 2008 can be explained in part by a stronger than normal subtropical Atlantic high pressure system (STH) in 2009 compared to 2008. Changes in the strength of the STH account for part of the NAO variability, along with changes in atmospheric circulation in the subpolar Atlantic (Wallace and Gutzler 1981). It is therefore possible for strong fluctuations in the STH to occur without corresponding fluctuations in the NAO index if the STH and subpolar Atlantic vary in phase. Indeed, the STH was 1.5 standard deviations above normal in January 2009, compared to one standard deviation below normal in January 2008 despite positive values of the NAO index in both years (Table 1). The strong influence of the STH on TNA wind speed during 2008–09, independent of the NAO and ENSO, is consistent with a statistical analysis for 1982–2009. Multiple linear regression using the NAO, Niño-3.4, and STH indices explains 80% of tropical North Atlantic wind speed variance in January, compared to 55% when the predictors are limited to the NAO and Niño-3.4 indices. The persistence of strong positive wind speed anomalies from January to February 2009 despite a negative NAO index and weakly positive STH may be due to stronger than normal convection in the Amazon during February 2009 (Table 1), consistent with Enfield and Mayer (1997) and Saravanan and Chang (2000).

The development of cold SST anomalies in the TNA in January coincident with stronger than normal trade winds suggests that the SST anomalies here were forced primarily by enhanced wind-induced evaporative heat loss, consistent with previous studies (Cayan 1992, Carton et al. 1996; Tanimoto and Xie 2002; Foltz and McPhaden 2006). Following the initial cooling in the TNA in January 2009, cold SST anomalies

11

persisted between 2°N–12°N during Feb–May 2009 despite much weaker wind speed anomalies in this region (Fig. 2b,c). This is the time of year when positive wind-evaporation-SST feedback is strongest in the tropical Atlantic (Xie and Carton 2004). It is therefore possible that positive wind-evaporation-SST (WES) feedback contributed to the strong anomalous cooling in the equatorial North Atlantic (ENA; 2°N–12°N, 15°W–45°W) and rapid development of the AMM during Feb–May 2009. In the next two sections we analyze the processes responsible for the generation and persistence of the cold SST anomalies in the ENA during Jan–Apr 2009.

3.2 Ekman pumping and entrainment anomalies

Previous studies suggest that on interannual timescales SST anomalies in the TNA (12°N–25°N) are driven primarily by changes in wind-induced latent heat flux. In contrast, in the equatorial band (12°S–12°N) surface heat fluxes appear to be less important relative to ocean dynamics (Carton and Huang 1994; Carton et al. 1996). Therefore, we expect that ocean dynamics may have contributed significantly to the development of the cold SST anomalies in this region during January–May 2009. One candidate is anomalous Ekman pumping, driven by anomalous northwesterly winds in the equatorial Atlantic (Fig. 2). Foltz and McPhaden (2010a) showed that the anomalous northwesterlies in early 2009 generated upwelling equatorial Rossby waves, which in addition to Ekman pumping, may have contributed to anomalous cooling of SST. In this section we first focus on the role of Ekman pumping, a mechanism that was not considered by Foltz and McPhaden (2010a). We then discuss entrainment, which implicitly includes the contributions from equatorial waves and Ekman dynamics.

To calculate Ekman pumping velocity, we first follow Lagerloef et al. (1999) and assume a steady linear momentum balance in the upper ocean:

$$-fh_ev_e = \frac{\tau^x}{\rho} - ru_e \tag{1}$$

$$fh_eu_e = \frac{\tau^y}{\rho} - rv_e \tag{2}$$

Here h_e is a constant depth of 30 m and r is a frictional damping coefficient set to 2×10^{-4} m s^{-1}. The values of h_e and r were determined empirically from the motion of surface drifting buoys in the global equatorial ocean (Lagerloef et al. 1999). Ekman pumping velocity is then calculated from (1) and (2) as the divergence of the Ekman transport:

$$
\begin{aligned}
w_e &= h_e \nabla \cdot \mathbf{v_e} \\
&= \frac{-2rh_e^3 f \beta \tau^y}{\rho(r^2 + h_e^2 f^2)^2} + \frac{h_e^2 f \frac{\partial \tau^y}{\partial x} + rh_e \frac{\partial \tau^y}{\partial y}}{\rho(r^2 + h_e^2 f^2)} \\
&+ \frac{2h_e^3 f^2 \beta \tau^x}{\rho(r^2 + h_e^2 f^2)^2} + \frac{-h_e^2 f \frac{\partial \tau^x}{\partial y} + rh_e \frac{\partial \tau^x}{\partial x} - h_e^2 \beta \tau^x}{\rho(r^2 + h_e^2 f^2)}
\end{aligned}
\tag{3}
$$

In most of the tropical Atlantic, poleward of 10° and away from from the African coast, climatological Ekman pumping is weak and negative (i.e., downwelling) during Jan–Apr (Fig. 3a). Ekman pumping (i.e., upwelling) of less than 0.3 m day^{-1} is present in the eastern basin poleward of 5°. There is a narrow band of stronger Ekman pumping (>1 m day^{-1}) centered just south of the equator and a band of strong negative values just north of the equator in the eastern basin.

During boreal winter and spring 2009 there was Ekman pumping of $\sim$0.3–1.5 m day^{-1} between the equator and 6°N, west of 20°W, in a region where there is normally negative Ekman pumping (i.e., downwelling) or very weak upwelling (Fig. 3b). Ekman pumping anomalies in Jan–Apr 2009 reached 1 m day^{-1} in a narrow band centered near 3°N between 20°W–40°W. Anomalous Ekman pumping here was driven

13

primarily by the meridional component of wind stress (Fig. 3c). Anomalous northerly wind stress acting on the meridional gradient of planetary vorticity (the beta effect; first term on the right in (3)), combined with the westward increase in anomalous northerly wind stress (the curl effect; second term on the right in (3)) and anomalous meridional wind stress divergence (third term on the right in (3)), all contributed to positive Ekman pumping anomalies between the equator and 6°N. The strongest Ekman pumping anomalies coincided with anomalous shoaling of the thermocline of ~10 m (Fig. 4d-f).

During Jan–Feb, there was also pronounced anomalous deepening of the mixed layer between the equator and 30°N (Fig. 4d-f), which was most likely driven by enhanced turbulent mixing associated with the anomalously strong trade winds during the same period (Fig. 2a, Fig. 3c). The anomalous mixed layer deepening was strongest to the north of the strongest Ekman pumping and thermocline depth anomalies, where the wind speed anomalies were greatest.

The anomalous Ekman pumping and mixed layer deepening would have tended to cool SST anomalously through entrainment. Entrainment velocity here is defined following McPhaden (1982):

$$w_{entr} = \frac{\partial h}{\partial t} - \frac{\partial Z_{20}}{\partial t} \tag{4}$$

In (4), h is the mixed layer thickness and Z_{20} is the depth of the 20°C isotherm, defined here as positive downward. Positive entrainment, which tends to cool the mixed layer, will occur when w_{entr} is positive (e.g., when the mixed layer deepens faster than the thermocline or shoals more slowly). The climatological entrainment velocity is positive between the equator and 10°N during January–February, when the mixed layer is

14

deepening to the west of 30°W, and Z_{20} is shoaling in the east (Fig. 4a-c). The strongest anomalous entrainment velocity in 2009 also occurs in this region and during January–February, the period with anomalous mixed layer deepening and anomalous shoaling of the thermocline (Fig. 4d-f).

The efficiency with which anomalous entrainment velocity cools SST depends on the vertical temperature gradient at the base of the mixed layer and the mixed layer depth:

$$\left(\frac{\partial T}{\partial t}\right)_{entr} = -\frac{H\Delta T w_{entr}}{h} \tag{5}$$

Here H is the Heaviside unit funtion (H=0 if w_{entr} <0 and H=1 otherwise), T is the vertically-averaged mixed layer temperature, and ΔT is the temperature jump at the base of the mixed layer. Based on (5), we anticipate that the strongest entrainment will occur in the eastern basin, since this is where the mixed layer is thinnest on average, thus reducing its heat capacity, and where the thermocline is shallowest, tending to increase the magnitude of ΔT (Fig. 4a-c). We expect entrainment to have the strongest impact on SST in a climatological sense during Jan–Feb, when w_{entr} is positive. Similarly, we expect the strongest anomalous entrainment cooling in 2009 to occur in the eastern basin and during January–February, when anomalous entrainment velocity is strongest. The results of this qualitative analysis are generally consistent with the location and timing of the strongest anomalous cooling of SST in the tropical North Atlantic during 2009 (Fig. 5a).

3.3 Mixed layer temperature balance

In order to quantify the contributions from entrainment and surface heat fluxes to the anomalous cooling in early 2009, we consider the mixed layer temperature budget, which can be written

$$\frac{\partial T'}{\partial t} = \frac{Q_0'}{\rho c_p (\overline{h} + h')} - \frac{\overline{Q_0} h'}{\rho c_p (\overline{h} + h')^2} - (\mathbf{v} \cdot \nabla T)' - \left(\frac{H \Delta T w_{entr}}{h} \right)' + \epsilon \qquad (6)$$

Here overbars indicate the mean seasonal cycle and primes indicate anomalies from the monthly mean seasonal cycle. The term on the left is the change in mixed layer temperature. The first four terms on the righthand side are the changes in mixed layer temperature due to anomalies of the surface heat flux (Q_0), anomalies of mixed layer thickness acting on the mean surface heat flux, horizontal temperature advection, and entrainment, respectively, and ϵ represents the sum of errors in the estimation of the other terms in (6) and unresolved processes, such as anomalies of vertical turbulent diffusion at the base of the mixed layer. Here T is vertically averaged temperature in the mixed layer, h is the mixed layer thickness, and $\mathbf{v}$ is horizontal velocity averaged vertically in the mixed layer. We parameterize the temperature jump at the base of the mixed layer in the entrainment term as $\Delta T = T - T_{h|10}$, where $T_{h|10}$ is the temperature 10 m below the base of the mixed layer. This parameterization gives $\Delta T = 2°C$ averaged between 2°N–12°N during January–April, which is consistent with ΔT used in previous studies (e. g., Hayes et al. 1991, Foltz et al. 2010). In reality, ΔT likely depends on a number of factors, such as stratification below the mixed layer and the magnitude of w_e. We therefore anticipate a relatively high degree of uncertainty in our estimates of entrainment. For terms on the righthand side of (6) we have retained the

16

nonlinear components since anomalies of h can be nearly as large as seasonal mean values of h.

We calculate T from monthly averaged TMI/AMSR-E SST. Individual Argo temperature and salinity profiles during 2005–2009 are used to calculate monthly averaged h, ΔT, and Z_{20}. The mixed layer depth is calculated using the criterion of the density equivalent of a 0.3°C decrease from a depth of 5 m. Results are similar for criteria ranging from 0.2–0.5°C. The net surface heat flux consists of the latent, sensible, shortwave, and longwave heat fluxes. The shortwave and longwave components are obtained from the TropFlux analysis. We calculate the amount of SWR penetrating through the base of the mixed layer as $Q_{pen} = 0.47 Q_{sfc} e^{-h/15}$, where Q_{sfc} is the net surface SWR assuming an albedo of 6%.

The latent and sensible heat fluxes are calculated using bulk flux formulations with NCEP/NCAR reanalysis air temperature and specific humidity, TMI/AMSR-E SST, and QuikSCAT wind speed: $Q_e = \rho_a L C_e s(q_s - q)$, $Q_s = \rho_a c_p C_h s(T_s - T)$. Here s is wind speed, q_s is saturation specific humidity at the sea surface calculated from SST, q is specific humidity, T_s is SST, T is air temperature, and $C_e = C_h = 1.5 \times 10^{-3}$. This hybrid satellite-reanalysis approach is used because of significant errors in the reanalysis wind speed and turbulent heat fluxes (e.g., Sun et al. 2003). The longwave and sensible heat fluxes are generally weak compared to the latent and shortwave components. Anomalies of horizontal temperature advection are calculated from satellite-derived OSCAR currents and satellite SST gradients. We use the convention that a positive surface heat flux tends to warm the ocean. Error estimates for the anomalous change in T and the sum of the terms on the righthand side of (6) are shown in Table 2 and discussed in the Appendix.

During Jan–Feb 2009, anomalous cooling of SST was strongest between the equator and $\sim 15°$N (Fig. 5a). The cooling was driven primarily by stronger than normal latent heat flux (LHF) and entrainment (Fig. 5b-e). In Mar–Apr, there was additional anomalous cooling in the 2°N–12°N band and anomalous warming to the north and south (Fig. 5f). Anomalies of LHF and $h'\overline{Q_0}$ contributed to the anomalous warming outside of the 2°N–12°N band during Mar–Apr (Fig. 5g,j). Between 2°N–12°N, anomalous cooling from entrainment and $h'\overline{Q_0}$ was balanced by strong anomalous warming from LHF and shortwave radiation (SWR). Horizontal temperature advection tended to cool the mixed layer anomalously in the eastern basin between 5°N–15°N, where westward mean currents and anomalous zonal SST gradients were strongest. Averaged in the tropical North Atlantic, however, its contribution to the anomalous cooling was small compared to surface fluxes and entrainment.

We next focus on the equatorial North Atlantic (ENA) region (2°N–12°N, 15°W–45°W) for a quantitative assessment of the mixed layer temperature balance. Our selection of this region is based on several factors. First, the SST anomalies in this region were generally much stronger than those to the north and south. The processes responsible for generating the SST anomalies in this region are therefore more likely to be resolved above observational noise and uncertainties associated with uneven sampling. Second, based on our qualitative analysis, the temperature budget in the ENA region appears to be a balance between several terms, including entrainment, LHF, SWR, and $h'\overline{Q_0}$. Quantifying these terms in relation to anomalous changes in SST will help to determine which processes are most important. Finally, the ENA region is sampled by a larger number of Argo floats compared to the equatorial band, and there are two PIRATA moorings in the ENA region that were well positioned to record the

18

strong anomalies in early 2009 (Fig. 2, section 4).

Because of strong spatial variability of the temperature budget in the ENA (Fig. 5), we calculate the terms in (6) averaged in four subregions (**NE**: 15°W–30°W, 7°N–12°N; **NW**: 30°W–45°W, 7°N–12°N; **SW**: 30°W–45°W, 2°N–7°N; **SE**: 15°W–30°W, 2°N–7°N) and then average each of the subregions to obtain the temperature balance in the ENA region as a whole.

During January–February both wind-induced latent heat flux (LHF) and entrainment contributed significantly to the observed cooling in the ENA region (Table 2). Anomalous cooling from entrainment was comparable in magnitude to that from wind-induced LHF and was driven by anomalous mixed layer deepening in the NW, NE, and SW subregions, and thermocline shoaling in the SE subregion. The strongest anomalies of entrainment cooling were concentrated in the eastern basin (NE and SE subregions; Fig. 5d), where there is a shallow mean mixed layer and thermocline (Fig. 4b). Anomalous cooling from wind-induced LHF was strongest in the NE subregion (Fig. 5b), where the wind speed anomaly was strongest and the climatological mixed layer is thinnest. The good agreement between the sum of LHF, SWR, and entrainment and the observed change in SST suggests that other processes, such as horizontal temperature advection and vertical turbulent mixing, were relatively unimportant, or that they canceled one another (Table 2).

After the initial anomalous cooling of 1°C in January–February, subsequent cooling during March–April was relatively weak. The weaker cooling during March–April is a consequence of an anomalous warming tendency of 0.7°C due to LHF-induced damping of the anomalously cold SST, combined with a warming tendency of 0.7°C from the enhanced SWR associated with the southward anomalous displacement of the

19

ITCZ (Fig. 5f-h; Table 2). The LHF-induced anomalous warming is partially balanced by a cooling tendency from entrainment, combined with anomalous cooling from the dilution of the mean positive surface heat flux over a thicker mixed layer (i.e., a reduction in the ability of the surface flux to warm SST due to the increased volume of the mixed layer) (Fig. 5i,j).

The sum of the LHF, SWR, surface heat flux dilution, and entrainment terms contributed anomalous warming of 0.9°C during March–April, whereas the observed SST decreased by 0.2°C (Table 2). It is therefore possible that horizontal temperature advection played an important role during this period. It is also possible that we have underestimated entrainment due to our simple parameterization of ΔT or because of uneven sampling from Argo floats. First we consider horizontal temperature advection.

Following Lee et al. (2004), the anomalous change in mixed layer temperature in the ENA region due to horizontal advection can be expressed as

$$\left(\frac{\partial T}{\partial t}\right)'_{adv} = \frac{(u_w \delta T_w)' - (u_e \delta T_e)'}{\Delta x} + \frac{(v_s \delta T_s)' - (v_n \delta T_n)'}{\Delta y} \tag{7}$$

Here u and v are zonal and meridional velocity from OSCAR, respectively, δT is the difference between SST and SST averaged in the ENA region, and Δx and Δy are the distances along the zonal and meridional boundaries of the ENA region, respectively. The subscripts w, e, s, and n represent averages along the western, eastern, southern, and northern boundaries, respectively. Based on (7), we find that zonal advection tended to cool the mixed layer anomalously by 0.2°C between Jan–Apr 2009, with most of the cooling occurring during Mar–Apr. In contrast, meridional advection provided weak (<0.1°C) anomalous warming between Jan–Apr. As a result, horizontal advection tended to cool the mixed layer by only 0.1°C during March–April, whereas

the temperature balance residual during this period indicates cooling of 1.1°C is needed to close the budget.

It is also possible that we have underestimated entrainment during March–April. Our estimates are based on Argo profiles, which are unevenly distributed spatially. The band of anomalous Ekman pumping during March–April 2009 is concentrated in a narrow latitude range centered near 3°N (Fig. 3c) that was undersampled by Argo floats relative to the northern portion of the ENA region. During March–April 2009 there were 124 Argo profiles between 4°N–7°N, but only 30 profiles between 2°N–4°N. The possibility that we have underestimated entrainment is also supported by the results of a temperature budget analysis at the 4°N, 23°W PIRATA mooring location presented in the next section, which shows anomalous mixed layer cooling of ∼2°C during March–April 2009 associated with the anomalous vertical heat flux at the base of the mixed layer. The spatial distribution of Argo floats is similar during January–February 2009, suggesting that we may have underestimated entrainment during this period as well.

In summary, the anomalous cooling in the equatorial North Atlantic (2°N–12°N) during January–February 2009 was driven by a combination of enhanced wind-induced latent heat loss and entrainment. After the initial cooling, SSTs remained anomalously cold during March and April due to a balance between the dilution of the surface heat flux over a thicker mixed layer, tending to cool the mixed layer anomalously, and the combination of anomalous warming from enhanced SWR due to the anomalous southward shift of the ITCZ, and SST-induced evaporation, tending to damp the cold anomaly back to climatology. Failure to close the temperature balance during March–April likely results from an underestimation of entrainment cooling during this period.

4 PIRATA mooring locations

In this section we analyze the mixed layer temperature balances at two PIRATA mooring locations in the ENA region (12°N, 23°W and 4°N, 23°W) (Fig. 2c,d). The advantages of using measurements from the moorings are the increased temporal resolution of subsurface temperature and salinity measurements (daily from the moorings versus monthly from Argo) and more accurate measurements of surface fluxes from the moorings compared to satellites and atmospheric reanalyses. The temperature budgets at the mooring locations therefore complement the area-averaged analysis presented in the previous section.

The mixed layer temperature balance equation applied at the mooring locations is similar to that used for the area-averaged analysis (eq. 6):

$$\frac{\partial T'}{\partial t} = \left(\frac{Q_0}{\rho c_p h}\right)' + Q'_{ocean} \tag{8}$$

$$Q'_{ocean} = -\left(\mathbf{v} \cdot \nabla T\right)' - \left(\frac{H \Delta T w_{entr}}{h}\right)' + \epsilon \tag{9}$$

Here all terms are as in (6). Terms in (8) are defined as positive when they tend to heat the mixed layer. Mixed layer thickness, ΔT, Z_{20}, entrainment, and the penetrative component of shortwave radiation (SWR) are calculated as in section 3.3 using daily averages of buoy temperature, salinity, and surface shortwave radiation. Mixed layer temperature is calculated using buoy subsurface temperature and mixed layer depth. Mixed layer depth is estimated using the criterion of the density equivalent of 0.3°C temperature decrease from a depth of 1 m.

Horizontal advection (first term on the right in eq. 9) is calculated using daily OSCAR currents and TMI/AMSR-E SST. The OSCAR zonal currents agree reasonably

22

well with zonal currents at a depth of 10 m from the moorings. The meridional currents are more poorly represented by OSCAR. The correlation between 5-day averaged buoy and OSCAR zonal velocity at 12°N, 23°W is 0.7, based on ~2 years of daily data. The record-length mean is -6.7 cm s^{-1} for OSCAR and -3.8 cm s^{-1} for the mooring. For the meridional component the correlation is 0.4, and the mean of the mooring velocity is 2.0 cm s^{-1}, while for OSCAR the mean is -0.1 cm s^{-1}. At 4°N, 23°W the correlation for the zonal component is 0.8, and for the meridional component the correlation is zero. The record-length means for the zonal component are 8.3 cm s^{-1} for the mooring and 6.3 cm s^{-1} for OSCAR. For the meridional component the means are 3.3 cm s^{-1} for the mooring and 0 cm s^{-1} for OSCAR. These uncertainties in OSCAR currents translate to errors in the temperature balance of $\pm 0.1 - 0.2$°C mo^{-1} (see Appendix).

The surface latent and sensible heat fluxes are calculated using daily buoy air temperature, relative humidity, SST, and wind speed in version 3 of the COARE bulk flux algorithm (Fairall et al. 2003). We use daily TropFlux net longwave radiation (LWR) at 4°N, 23°W and calculate net longwave emission at 12°N, 23°W using direct measurements of downward LWR at the mooring. Because of gaps in the buoy time series, anomalies for the Nov 2008 – Nov 2009 period are calculated with respect to either the same period during 2007–2008 (at 12°N, 23°W) or 2006–2007 (4°N, 23°W). Error estimates for each term in (8) and (9) are discussed in the Appendix, and error bars for Q_{ocean} and horizontal advection (the terms with the largest errors) are shown in Figs. 6–7.

4.1   12°N, 23°W

The PIRATA mooring at 12°N, 23°W was located to the northwest of the strongest cold SST anomalies in March–May 2009 (Fig. 2b,c). There was strong anomalous

23

cooling at this location during Jan–Feb 2009, consistent with satellite SSTs during the same period (Fig. 6a). The anomalous cooling at the mooring location corresponds to a period with stronger than normal wind speed and a pronounced anomalous deepening of the mixed layer (Fig. 6b). The timing and magnitude of the anomalous mixed layer deepening and wind speed anomalies are consistent with satellite and Argo measurements in the ENA region (Figs. 2, 4).

Enhanced wind speed in Jan–Feb at 12°N, 23°W tended to cool the mixed layer anomalously through enhanced latent heat flux (LHF). However, when anomalies in mixed layer depth are taken into account, the net impact of LHF on SST during Jan–Apr was anomalous warming due to the dilution of the climatological latent heat loss over a thicker mixed layer (Fig. 6c). The same mechanism played an important role in determining the sign of the SWR-induced SST tendency. There was anomalously strong SWR during mid January through April 2009, tending to warm the mixed layer anomalously. Dilution of the climatological SWR flux over a thicker mixed layer, however, resulted in a net anomalous cooling tendency due to SWR during Jan–Apr (Fig. 6c). Overall, there was anomalous mixed layer cooling of 1°C between March and April 2009 associated with the dilution of the mean positive surface heat flux over the anomalously thick mixed layer (Fig. 6d). The anomalous cooling associated with the thicker mixed layer is consistent with the cooling observed in the ENA region during the same period (Table 2), though the cooling at the mooring location is significantly stronger. The stronger cooling at the mooring location compared to the ENA region is likely due to the combination of a larger positive climatological net surface heat flux and stronger anomalous mixed layer deepening at the mooring location.

The net surface heat flux agrees reasonably well with the rate of change of mixed

24

layer temperature during late 2008 and early 2009 at 12°N, 23°W (Fig. 6d), though there was stronger anomalous cooling during Jan–Feb 2009 than predicted by the surface heat flux (Fig. 6d,e). The mismatch can be explained by an anomalous cooling tendency from zonal temperature advection associated with an anomalously strong negative zonal SST gradient (i. e., strongest anomalous cooling located to the east of the mooring) in combination with climatological westward near-surface currents. Entrainment was not significant at this location, consistent with weak climatological downwelling and a deeper than normal thermocline. In the previous section it was found that entrainment was important in the NE subregion (7°N–12°N, 15°W–30°W) during Jan–Feb. The difference likely results from the positioning of the PIRATA mooring on the northern edge of the NE subregion, combined with a southward increase in the strength of Ekman pumping, thermocline depth, and entrainment anomalies (Figs. 3c, 4, 5).

4.2   4°N, 23°W

The PIRATA mooring at 4°N, 23°W is located in the southeastern corner of the ENA region, where there was strong anomalous cooling and anomalous Ekman pumping during Jan–Mar 2009 (Figs. 3c, 4, 5). The maximum negative SST anomaly occurred in late April at this location, almost two months after the strongest cold anomaly at 12°N, 23°W (Fig. 7a). Anomalous Ekman pumping led to anomalous shoaling of the thermocline of ∼30 m between January and mid May at 4°N, 23°W (Fig. 7b). This timing is consistent with that found in the ENA region (Fig. 4). The largest thermocline depth anomalies at 4°N, 23°W coincided with the period when the thermocline is shallowest climatologically at this location.

Stronger than normal wind speed during Jan–Mar 2009 at 4°N, 23°W tended

25

to cool the mixed layer anomalously through enhanced latent heat loss (Fig. 7c), consistent with the area-averaged temperature budget in the ENA region (Table 2). Anomalous cooling from latent heat loss during Feb–May 2009 was balanced by a strong anomalous warming tendency associated with positive anomalies of SWR (Fig. 7c). The enhanced SWR at the mooring location during Feb–June is consistent with the large-scale analysis of the previous section (Fig. 5c,h) and the pronounced anomalous southward shift of the ITCZ during Apr–May 2009 (Fig. 1b).

The net surface heat flux agrees reasonably well with the mixed layer temperature tendency during late 2008 and early 2009, though there is a period in April with strong anomalous cooling ($\sim 2°C$ mo^{-1}) that cannot be explained by the surface heat flux (Fig. 7d,e). April is also the month with the strongest observed anomalous cooling, strong Ekman pumping anomalies, shallower than normal thermocline, and the climatological minimum in thermocline depth. It is therefore anticipated that entrainment was important at the mooring location in April. Indeed, estimates from the mooring data show a broad peak of anomalous entrainment cooling centered in early April (Fig. 7e). The presence of strong entrainment cooling at 4°N, 23°W is consistent with the analysis based on Argo profiles, which shows a maximum in entrainment cooling in the NE and SE subregions (2°N–12°N, 15°W–30°W) and maximum thermocline shoaling in the SE subregion (2°N–7°N, 15°W–30°W) (Figs. 4, 5). The timing of the strongest entrainment cooling is inconsistent with the temperature budget in the ENA region, however, which shows a maximum in Jan–Feb (Table 2). The discrepancy is likely due in part to the uneven spatial distribution of Argo floats in the ENA region, as discussed in the previous section.

26

5   Summary and Discussion

In Jan–May 2009 a strong Atlantic meridional mode event developed in the tropical Atlantic. During its peak in boreal spring, there were cold SST anomalies of 0.5°–2°C in the equatorial North Atlantic (2°N–12°N) and weaker warm SST anomalies in the equatorial South Atlantic (0°–5°S). In this study the causes of the strong anomalous cooling in the equatorial North Atlantic are analyzed using satellite and in situ data sets.

It is found that the cooling was initiated in January by an anomalous intensification of the subtropical North Atlantic high pressure system and associated increase in strength of the trade winds in the tropical North Atlantic (12°N–25°N). Stronger than normal trade winds persisted through February, due in part to a moderate La Niña in the Pacific and anomalously strong convection in the Amazon. Cold SST anomalies formed first near 20°N off the coast of Africa, progressed southward to 2°N-12°N, then intensified and expanded westward during Feb–May. Surface winds in the equatorial Atlantic responded to the meridional SST gradient, becoming northwesterly in January and intensifying through May, consistent with positive wind-evaporation-SST feedback.

The surface wind anomalies forced anomalous Ekman pumping between 2°N–6°N, shoaling the thermocline anomalously by 10–30 m during Jan–May. Farther north (6°N–12°N), stronger than normal trade winds induced anomalous mixed layer deepening of 5–20 m. In each region, the net effect was to bring the thermocline closer to the base of the mixed layer, enhancing entrainment cooling. The anomalous entrainment cooling was partially balanced by positive anomalies of shortwave radiation associated with the pronounced anomalous southward shift of the ITCZ in response

27

to the interhemispheric SST gradient anomaly. Stronger than normal wind-induced evaporative heat loss also contributed significantly to the observed cooling in Jan–Feb. Dilution of the positive surface heat flux over an anomalously deep mixed layer (i.e., a reduction in the ability of the surface flux to warm SST due to the increased volume of the mixed layer) tended the cool the mixed layer anomalously during Mar–Apr 2009. The mechanisms responsible for generating the SST anomalies in the equatorial North Atlantic during Jan–Apr 2009 are summarized schematically in Fig. 8.

Our results for the event in 2009 are consistent with previous studies, which indicate that surface heat flux anomalies drive most of the interannual and decadal variability of SST in the northern tropical Atlantic, while ocean dynamics play an important role within 10° of the equator (Carton et al. 1996, Tanimoto and Xie 2002, Foltz and McPhaden 2006). We also found that changes in mixed layer depth affect the efficiency with which the net surface heat flux warms the mixed layer. It is interesting to compare our results to the mechanism proposed by Doi et al. (2010). They showed that changes in mixed layer depth in the Guinea Dome region (10°N–15°N, 20°W–35°W) during boreal fall affect the Atlantic meridional mode the following spring. Anomalous deepening of the mixed layer in the fall dilutes the negative surface heat flux in a thicker layer, tending to increase SST anomalously. In contrast, we find that anomalous deepening of the mixed layer in the spring dilutes the positive surface heat flux, tending to anomalously decrease SST. The opposite effects of changes in MLD on SST during fall and spring result from opposite signs of the net surface heat flux during these seasons.

We found that anomalous entrainment cooling in the 2°N–6°N band during Jan–Apr 2009 was driven in part by strong northwesterly wind anomalies and resultant

Ekman pumping. Foltz and McPhaden (2010a,b) showed that the wind stress field associated with a negative meridional mode in the spring (colder than normal SSTs north of the equator relative to the south, as occurred in 2009) generates upwelling equatorial Rossby waves north of the equator. The generation of upwelling Rossby waves is consistent with the observed southwestward propagation of the strongest cold SST anomalies during Jan–Apr 2009. Further studies are needed to quantify the contributions from Ekman dynamics and equatorial waves to thermocline depth and SST anomalies in the equatorial North Atlantic.

The results from this study suggest that there may be positive coupled feedbacks between Ekman pumping anomalies north of the equator and the cross-equatorial SST gradient anomaly. This feedback may act concurrently with positive wind-evaporation-SST (WES) feedback in the western Atlantic (Xie 1999, Chang et al. 2000). For example, after cold SST anomalies developed north of the equator in January 2009, north-westerly anomalous surface winds developed, causing anomalous Ekman pumping, shoaling of the thermocline, and cooling through entrainment. The anomalous cooling further intensified the cross-equatorial SST gradient anomaly, leading to stronger northwesterly wind anomalies. Both the WES feedback and Ekman pumping feedback are likely to be strongest in the boreal spring, when the thermocline is shallowest climatologically in the 2°N–12°N band and surface winds are most responsive to anomalies of the meridional SST gradient. Experiments with coupled models will be helpful for clarifying the relative importance of Ekman pumping, surface heat fluxes, and air-sea coupling for generating SST anomalies in the equatorial North Atlantic. As the observational records from Argo and PIRATA expand, it will also be possible to determine the extent to which the mechanisms at play in 2009 can be invoked to describe SST

29

643   variability in the equatorial North Atlantic in general.

Appendix: Error estimates

Satellite/Argo area-averages

Here we describe the methodology used to estimate errors for each term in the mixed layer temperature equation (5). Errors in the rate of change of mixed layer temperature are due to uncertainties in TMI/AMSR-E SST. We have estimated these errors to be $\pm 0.1°$C, based on the monthly RMS difference between TMI/AMSR-E SST and temperature at a depth of 1 m from the PIRATA moorings at 4°N, 38°W and 4°N, 23°W during 2003–2009.

Uncertainties in daily-averaged latent heat flux (Q_e) and surface shortwave radiation (SWR) are ± 20W m^{-2}, and for the net surface heat flux (Q_0) a value of ± 30W m^{-2} is used, following Kumar et al. (2011). These values are converted to monthly errors assuming an integral time scale (an estimate of the time period required to gain a new degree of freedom) of three days.

Errors in monthly Argo mixed layer depth (MLD), ΔT, and Z_{20} are calculated as the standard error of all measurements in a given equatorial North Atlantic (ENA) subregion for a given month. Typical errors are ± 5 m for mixed layer depth, 0.3°C for ΔT, and 5 m for Z_{20}.

Errors for each term in (5) averaged in each ENA subregion are calculated using the monthly errors for SST, Q_e, Q_0, SWR, MLD, ΔT, and Z_{20} and assuming the errors are uncorrelated in time. Errors for the ENA region are then calculated using the errors associated with each subregion, assuming two spatial degrees of freedom in the ENA region. The errors for the sum of the terms on the righthand side of (5) and the observed change in SST are shown in Table 2.

PIRATA moorings

Errors for each term in equation (6) are estimated using the methodology of Foltz and McPhaden (2009). Typical errors are 5–10 m for MLD and Z_{20}, 0.7°C mo^{-1} for latent heat flux, 0.1°C mo^{-1} for sensible heat flux, 0.1°C mo^{-1} for longwave radiation, 0.9°C mo^{-1} for absorbed shortwave radiation, and 1.4°C mo^{-1} for horizontal advection. Error estimates for shortwave radiation are likely underestimated at 12°N, 23°W since they do not include the effect of dust accumulation on the sensor (e.g., Foltz and McPhaden 2008). Visual inspection of the record at 12°N, 23°W did not reveal any obvious jumps in shortwave radiation immediately following sensor swaps, which generally indicates significant dust accumulation.

Acknowledgments

References

Adler, R. F., et al., 2003: The Version 2 Global Precipitation Climatology Project (GPCP) monthly precipitation analysis (1979–present). *J. Hydrometeorol.*, **4**, 1147–1167.

Bonjean, F., and G. S. E. Lagerloef, 2002: Diagnostic model and analysis of the surface currents in the tropical Pacific Ocean. *J. Phys. Oceanogr.*, **32**, 2938–2954.

Bourlès, B., et al., 2008: The PIRATA program: History, accomplishments, and future directions. *Bull. Am. Meteorol. Soc.*, **89**, 1111–1125.

Carton, J. A., and B. H. Huang, 1994: Warm events in the tropical Atlantic. *J. Phys. Oceanogr.*, **24**, 888–903.

Carton, J. A., X. H. Cao, B. S. Giese, and A. M. daSilva, 1996: Decadal and inter-annual SST variability in the tropical Atlantic Ocean. *J. Phys. Oceanogr.*, **26**, 1165–1175.

Cayan, D. R., 1992: Latent and sensible heat flux anomalies over the northern oceans - driving the sea surface temperature. *J. Phys. Oceanogr.*, **22**, 859–881.

Chang, P., R. Saravanan, L. Ji, and G. C. Hegerl, 2000: The effect of local sea surface temperatures on atmospheric circulation over the tropical Atlantic sector. *J. Climate*, **13**, 2195–2216.

Czaja, A., P. Van der Vaart, and J. Marshall, 2002: A diagnostic study of the role of remote forcing in tropical Atlantic variability. *J. Climate*, **15**, 3280–3290.

Doi, T., T. Tozuka, and T. Yamagata, 2010: The Atlantic meridional mode and its coupled variability with the Guinea Dome. *J. Climate*, **23**, 455–475.

Enfield, D. B., and D. A. Mayer, 1997: Tropical Atlantic sea surface temperature variability and its relation to El Niño Southern Oscillation. *J. Geophys. Res.*,

102, 929–945.

Fairall, C. W., E. F. Bradley, J. E. Hare, A. A. Grachev, and J. B. Edson, 2003: Bulk parameterization of air-sea fluxes: Updates and verification for the COARE algorithm, *J. Climate*, **16**, 571–591.

Foltz, G. R., J. Vialard, B. P. Kumar, and M. J. McPhaden, 2010: Seasonal mixed layer heat balance of the southwestern tropical Indian Ocean. *J. Climate*, **23**, 947–965.

Foltz, G. R., and M. J. McPhaden, 2006: The role of oceanic heat advection in the evolution of tropical North and South Atlantic SST anomalies. *J. Climate*, **19**, 6122–6138.

Foltz, G. R., and M. J. McPhaden, 2008: Impact of Saharan dust on tropical North Atlantic SST. *J. Climate*, **21**, 5048–5060.

Foltz, G. R., and M. J. McPhaden, 2009: Impact of barrier layer thickness on SST in the central tropical North Atlantic. *J. Climate*, **22**, 285–299.

Foltz, G. R., and M. J. McPhaden, 2010a: Abrupt equatorial wave-induced cooling of the Atlantic cold tongue in 2009. *Geophys. Res. Lett.*, **37**, L24605, doi:10.1029/2010GL045522.

Foltz, G. R., and M. J. McPhaden, 2010b: Interaction between the Atlantic meridional and Niño modes. *Geophys. Res. Lett.*, **37**, L18604, doi:10.1029/2010GL044001.

Giannini, A., R. Saravanan, and P. Chang, 2003: Oceanic forcing of Sahel rainfall on interannual to interdecadal time scales. *Science*, **302**, 1027–1030.

Gould, J., et al., 2004: Argo profiling floats bring new era of in situ ocean observations. *Eos, Trans AGU*, **85**, 179.

Hastenrath, S., and L. Greischar, 1993: Circulation mechanisms related to Northeast

733   Brazil rainfall anomalies. *J. Geophys. Res.*, **98**, 5093–5102.

734   Hayes, S. P., P. Chang, and M. J. McPhaden, 1991: Variability of the sea surface

735   temperature in the eastern equatorial Pacific during 1986–88. *J. Geophys. Res.*,

736   **96**, 10553–10566.

737   Hu, Z. Z., and B. H. Huang, 2006: Physical processes associated with the tropical

738   Atlantic SST meridional gradient, *J. Climate.* **19**, 5500–5518.

739   Huang, B. H., P. S. Schopf, and J. Shukla, 2004: Intrinsic ocean-atmosphere variability

740   of the tropical Atlantic Ocean. *J. Climate*, **17**, 2058–2077.

741   Kalnay, E., et al., 1996: The NCEP/NCAR 40-year reanalysis project. *Bull. Amer.*

742   *Meteor. Soc.*, **77**, 437–471.

743   Kumar, B. P., et al., 2011: TropFlux: Air-sea fluxes for the global tropical oceans –

744   description and evaluation against observations. *Climate Dynamics*, in revision.

745   Lagerloef, G. S. E., G. T. Mitchum, R. B. Lukas, and P. P. Niiler, 1999: Tropical

746   Pacific near-surface currents estimated from altimeter, wind, and drifter data. *J.*

747   *Geophys. Res.*, **104**, 23313–23326.

748   Lamb, P. J., 1978: Large-scale tropical Atlantic surface circulation patterns associated

749   with sub-Saharan weather anomalies. *Tellus*, **30**, 240–251.

750   Latif, M., N. Keenlyside, and J. Bader, 2007: Tropical sea surface temperature, ver-

751   tical wind shear, and hurricane development. *Geophys. Res. Lett.*, **34**, L01710,

752   doi:10.1029/2006GL027969.

753   Lee, T., I. Fukumori, and B. Tang, 2004: Temperature advection: Internal versus

754   external processes. *J. Phys. Oceanogr.*, **34**, 1936–1944.

755   Liebmann, B., and C. A. Smith, 1996: Description of a complete (interpolated) out-

756   going longwave radiation dataset. *Bull. Am. Meteorol. Soc.*, **77**, 1275–1277.

Lindzen, R. S., and S. Nigam, 1987: On the role of sea surface temperature gradients in forcing low-level winds and convergence in the tropics. *J. Atmos. Sci*, **44**, 2418–2436.

McPhaden, M. J., 1982: Variability in the central equatorial Indian Ocean Part II: Oceanic heat and turbulent energy balance. *Deep-Sea Res. I*, **52**, 495–518.

Nobre, C., and J. Shukla, 1996: Variation of sea surface temperature, wind stress, and rainfall over the tropical Atlantic and South America. *J. Climate*, **9**, 2464–2479.

Reynolds, R. W., N. A. Rayner, T. M. Smith, D. C. Stokes, and W. Q. Wang, 2002: An improved in situ and satellite SST analysis for climate. *J. Climate*, **15**, 1609–1625.

Saravanan, R., and P. Chang, 2000: Interaction between tropical Atlantic variability and El Niño-Southern Oscillation. *J. Climate*, **13**, 2177–2194.

Sun, B., L. Yu, and R. A. Weller, 2003: Comparisons of Surface Meteorology and Turbulent Heat Fluxes over the Atlantic: NWP Model Analyses versus Moored Buoy Observations. *J. Climate*, **16**, 679-695.

Tanimoto, Y., and S. P. Xie, 2002: Inter-hemispheric decadal variations in SST, surface wind, heat flux, and cloud cover over the Atlantic Ocean. *J. Meteor. Soc. Japan*, **80**, 1199–1219.

Wallace, J. M., and D. S. Gutzler, 1981: Teleconnections in the geopotential height field during the Northern Hemisphere winter. *Mon. Weather Rev.*, **109**, 784–812.

Wang, C. Z., D. B. Enfield, S. K. Lee, and C. W. Landsea, 2006: Influences of the Atlantic warm pool on Western Hemisphere summer rainfall and Atlantic hurricanes. *J. Clim.*, **19**, 3011–3028.

Xie, S.-P., 1999: A dynamic ocean-atmosphere model of the tropical Atlantic decadal

variability. *J. Climate*, **32**, 64–70.

Xie, S.-P., and J. A. Carton, 2004: Tropical Atlantic variability: Patterns, mechanisms, and impacts, in *Earths Climate: The Ocean-Atmosphere Interaction, Geophys. Monogr. Ser.*, vol. 147, edited by C. Wang, S.-P. Xie, and J. A. Carton, pp. 121 142, AGU, Washington, D. C.

Zhang, Y. W. B. Rossow, A. A. Lacis, V. Olnas, and M. I. Mishchenko, 2004: Calculation of radiative fluxes from the surface to top of atmosphere based on ISCCP and other global data sets: Refinements of the radiative transfer model and input data. *J. Geophys. Res.*, **109**, D19105, doi:10.1029/2003JD004457.

Figure Captions

Fig. 1 (a) Interannual anomalies of TMI/AMSR-E SST (shaded) and QuikSCAT wind velocity (vectors) averaged during April–May 2009. Wind vectors are plotted only where the magnitude of the wind speed anomaly is > 1 m s^{-1}. (b) Same as (a) except shading is GPCP rainfall anomaly. Here and in subsequent figures, anomalies are with respect to the 2003–2008 monthly mean seasonal cycle unless otherwise indicated. (c) Meridional SST gradient index (black line) averaged during Apr–May, calculated as Reynolds et al. (2002) SST anomaly averaged in the tropical North Atlantic minus South Atlantic (regions are indicated by boxes in (a)), and Apr–May Northeast Brazil rainfall (red line), calculated from GPCP averaged in boxed region shown in (b). Note that in (c) the values for each year include the record-length mean and are not anomalies as in (a) and (b). Black circle and red dot on the right in (c) are the record-length means of meridional SST gradient index and NE Brazil rainfall, respectively.

Fig. 2 Interannual anomalies of SST (shaded) and surface wind velocity (vectors) during 2009 for the months of (a) January, (b) March, (c) May, and (d) July. White boxes in (b) and (c) indicate equatorial North Atlantic (ENA) region used for temperature budget analysis. White dots in (b) and (c) are the positions of the PIRATA moorings used in this study.

Fig. 3 (a) 2003–08 climatologies of Ekman pumping velocity (shaded, >0 indicates upwelling) and wind stress (vectors) during January–April. (b) Jan–Apr 2009 Ekman

pumping velocity and wind stress. (c) Jan–Apr 2009 anomalies of Ekman pumping velocity and wind stress with respect to 2003–08 climatologies.

Fig. 4 Left column: Climatological (2003–08) mixed layer depth (red contours, with 60 m highlighted in bold) and depth of the 20°C isotherm (shading, with 80 m contoured in black) during Dec (a), Feb (b), and Apr (c). Right column: Same as left column, except contours are 2009 anomalies (with respect to 2005–08) of MLD, and shading represents 2009 anomalies of Z_{20}.

Fig. 5 Terms in the mixed layer temperature budget (eq. 5) averaged during Jan–Feb 2009 (left column) and Mar–Apr 2009 (right column). Negative values indicate anomalous cooling of SST. (a) and (f) Rate of change of SST. (b) and (g) Latent heat flux. (c) and (h) Surface shortwave radiation. (d) and (i) Entrainment, with contours shown for anomalies of 20°C isotherm depth (positive values for deeper than normal and negative values for shallower than normal). (e) and (j) Mixed layer depth (MLD) anomalies acting on the mean surface heat flux, with contours shown for MLD anomalies (positive for deeper than normal and negative for shallower than normal).

Fig. 6 Measurements from the PIRATA mooring at 12°N, 23°W during Nov 2008 – Jun 2009 (position of mooring is shown in Fig. 2). (a) SST anomaly. (b) Mixed layer depth (MLD) climatology (black) and 2008–09 anomaly (shading), and wind speed anomaly (red). (c) Anomalous contributions from surface latent heat flux (blue) and shortwave radiation absorbed in the mixed layer (red) to changes in SST. Thin blue line is the surface latent heat flux. (d) Anomalies of net surface heat flux (solid red),

838 surface heat flux with MLD held constant (dashed red), and mixed layer temperature

839 rate of change (black). (e) Anomalies of the sum of ocean processes (estimated from

840 the residual in the temperature balance and shown as solid blue curve), horizontal

841 temperature advection (green), and entrainment (pink). Blue and green shading rep-

842 resents one standard error. Anomalies are with respect to Nov 2007 – Jun 2008. Data

843 have been smoothed with a 20-day low-pass filter.

844

845 **Fig. 7** Same as in Fig. 6 except from the PIRATA mooring at 4°N, 23°W (loca-

846 tion shown in Fig. 2) and anomalies are with respect to Nov 2006 – Jun 2007. In

847 (b) the black curve is climatological 20°C isotherm depth (Z_{20}), grey shading is Z_{20}

848 anomaly, and red shading is Ekman pumping anomaly (positive values indicate up-

849 welling).

850

851 **Fig. 8** Schematic diagrams illustrating the processes responsible for generating the

852 SST anomalies during Jan–Apr 2009. Blue arrows in (a) represent anomalies of sur-

853 face wind velocity. In (b) the blue region is where anomalies of latent heat flux are

854 important, red is entrainment, green is anomalies of mixed layer depth acting on the

855 climatological surface heat flux, and grey shading is surface shortwave radiation.

Table Captions

Table 1 Climatic indices during Dec 2007 – Mar 2008 and Dec 2008 – Mar 2009. All values are monthly anomalies with respect to the corresponding 1982–2009 monthly means, normalized by the standard deviation. Tropical North Atlantic (TNA) wind speed is averaged 15°W–50°W, 5°N–20°N. North Atlantic Oscillation (NAO) index is NCEP/NCAR reanalysis surface pressure at the Azores minus Iceland. The Niño-3.4 index is SST averaged 120°W–170°W, 5°S–5°N. The subtropical high (STH) index is NCEP/NCAR reanalysis surface pressure averaged 30°W–40°W, 20°N–25°N. The Amazon convection index (Amzn) is satellite OLR averaged 30°W–70°W, 10°S–5°N. Negative values of OLR indicate enhanced convection. Bold font for Jan–Feb of each year highlights the months with the strongest positive wind speed anomalies in the TNA in 2009.

Table 2 2009 anomalies of terms in the mixed layer temperature balance, averaged in the ENA region (2°N–12°N, 15°W–45°W) during January–February (left column), March–April (middle), and the total for the January–April period (right column). The first row is the anomalous change in mixed layer temperature due to latent heat flux; second row due to anomalies of absorbed shortwave radiation; third row due to anomalies of mixed layer depth acting on the mean surface heat flux; and fourth row due to entrainment. Fifth row is the sum of the first three rows, and last row is observed (TMI/AMSR-E) anomalous change in SST. Units are °C. Errors for the sum and observed values are one standard error.
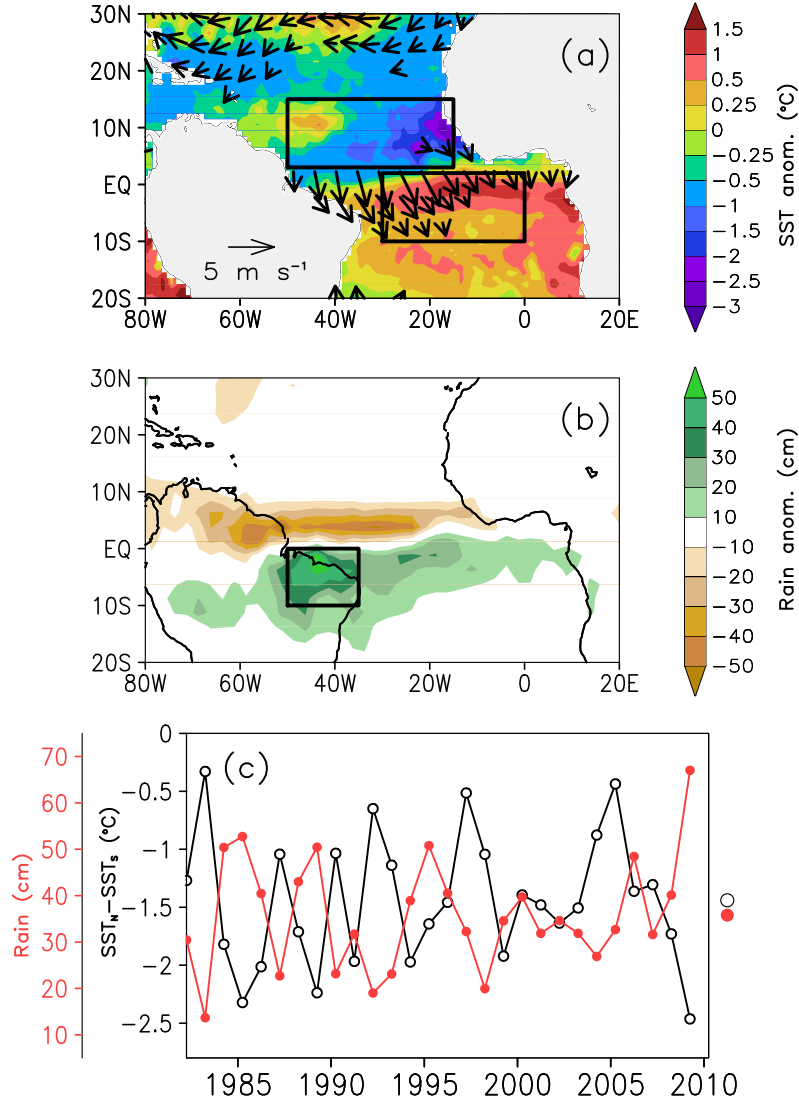
41

Fig. 1 (a) Interannual anomalies of TMI/AMSR-E SST (shaded) and QuikSCAT wind velocity (vectors) averaged during April–May 2009. Wind vectors are plotted only where the magnitude of the wind speed anomaly is > 1 m s^{-1}. (b) Same as (a) except shading is GPCP rainfall anomaly. Here and in subsequent figures, anomalies are with respect to the 2003–2008 monthly mean seasonal cycle unless otherwise indicated. (c) Meridional SST gradient index (black line) averaged during Apr–May, calculated as Reynolds et al. (2002) SST anomaly averaged in the tropical North Atlantic minus South Atlantic (regions are indicated by boxes in (a)), and Apr–May Northeast Brazil rainfall (red line), calculated from GPCP averaged in boxed region shown in (b). Note that in (c) the values for each year include the record-length mean and are not anomalies as in (a) and (b). Black circle and red dot on the right in (c) are the record-length means of meridional SST gradient index and NE Brazil rainfall, respectively
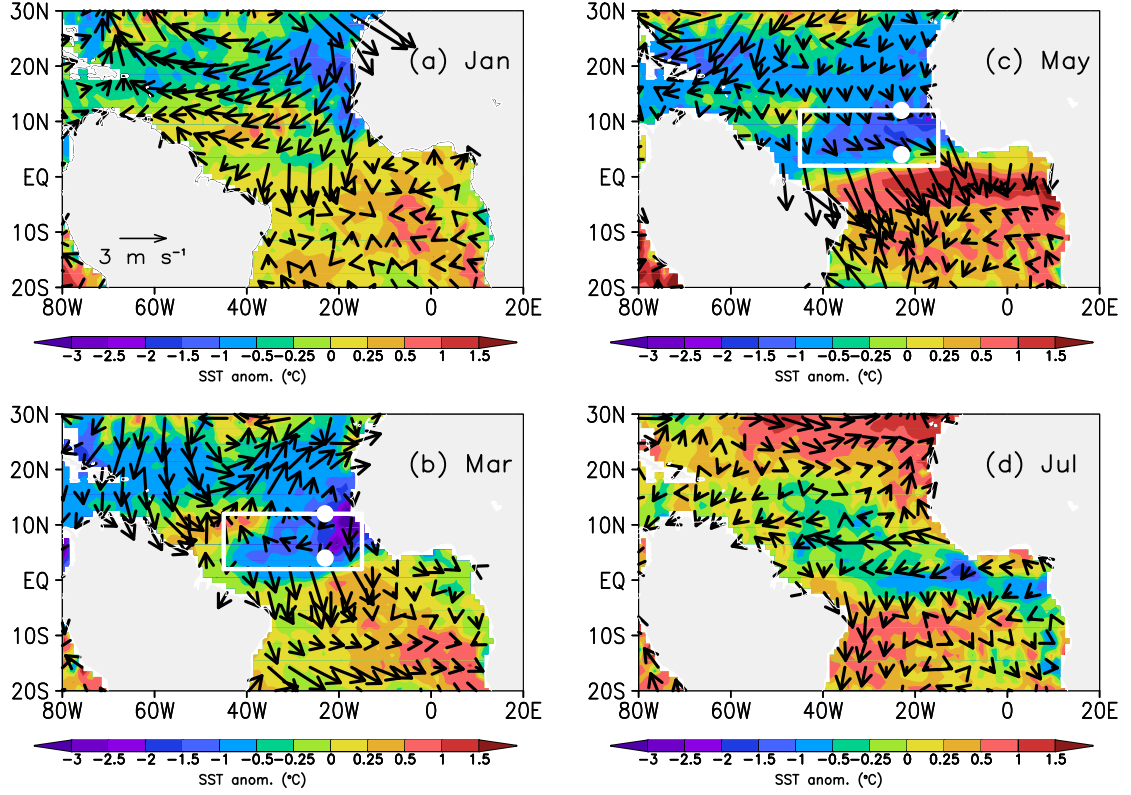
Fig. 2 Interannual anomalies of SST (shaded) and surface wind velocity (vectors) during 2009 for the months of (a) January, (b) March, (c) May, and (d) July. White boxes in (b) and (c) indicate equatorial North Atlantic (ENA) region used for temperature budget analysis. White dots in (b) and (c) are the positions of the PIRATA moorings used in this study.
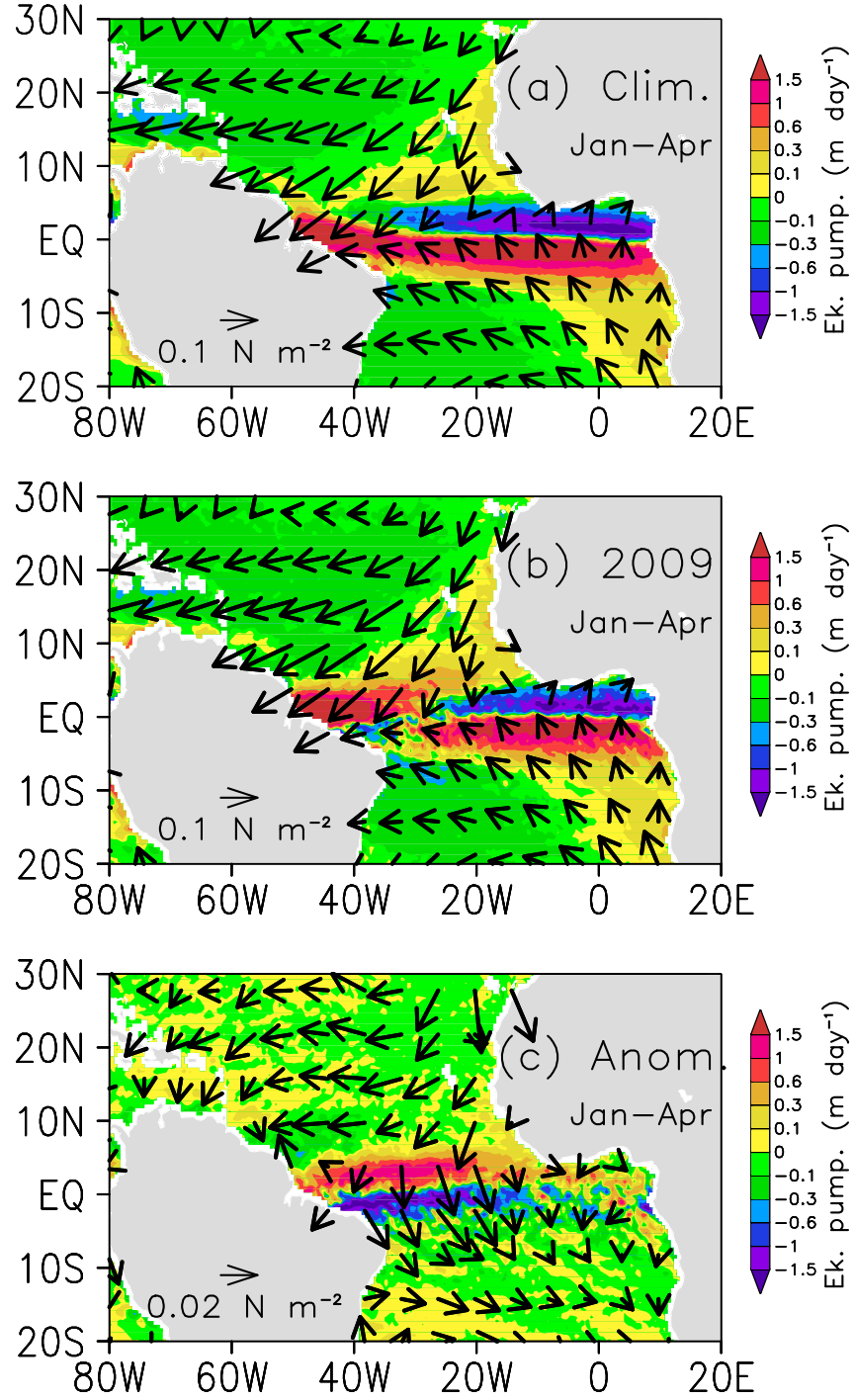
Fig. 3 (a) 2003–08 climatologies of Ekman pumping velocity (shaded, >0 indicates upwelling) and wind stress (vectors) during January–April. (b) Jan–Apr 2009 Ekman pumping velocity and wind stress. (c) Jan–Apr 2009 anomalies of Ekman pumping velocity and wind stress with respect to 2003–08 climatologies.
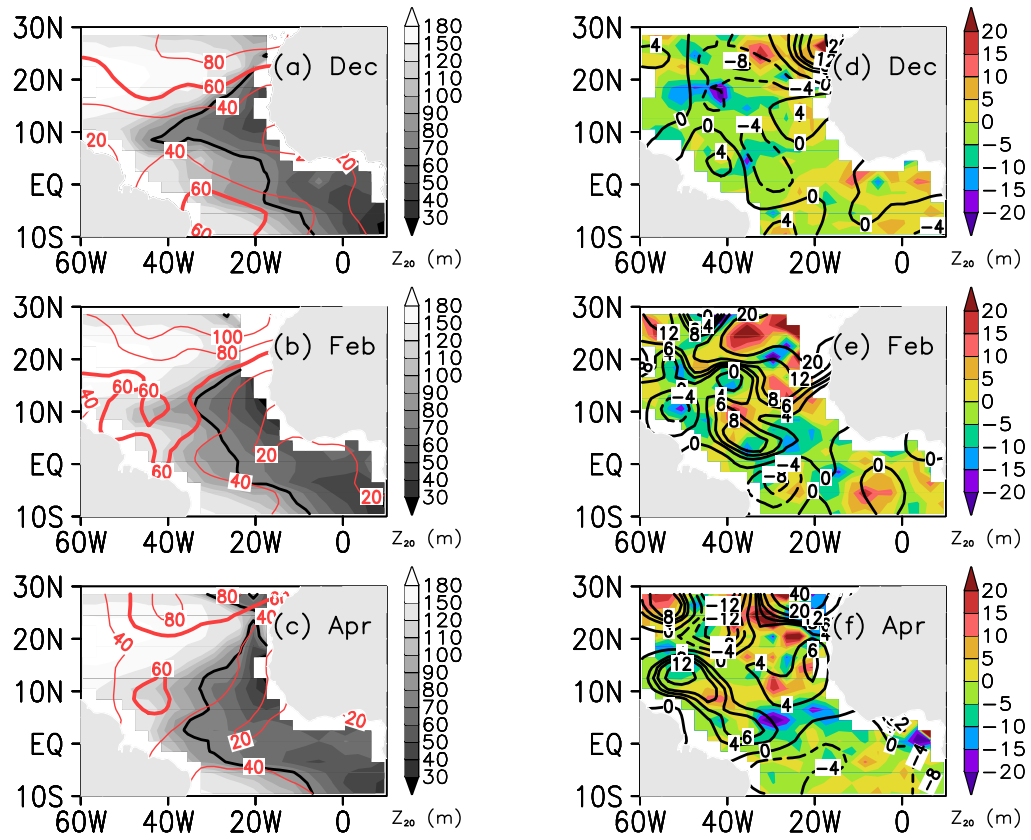
Fig. 4 Left column: Climatological (2003–08) mixed layer depth (red contours, with 60 m highlighted in bold) and depth of the 20°C isotherm (shading, with 80 m contoured in black) during Dec (a), Feb (b), and Apr (c). Right column: Same as left column, except contours are 2009 anomalies (with respect to 2005–08) of MLD, and shading represents 2009 anomalies of Z_{20}.
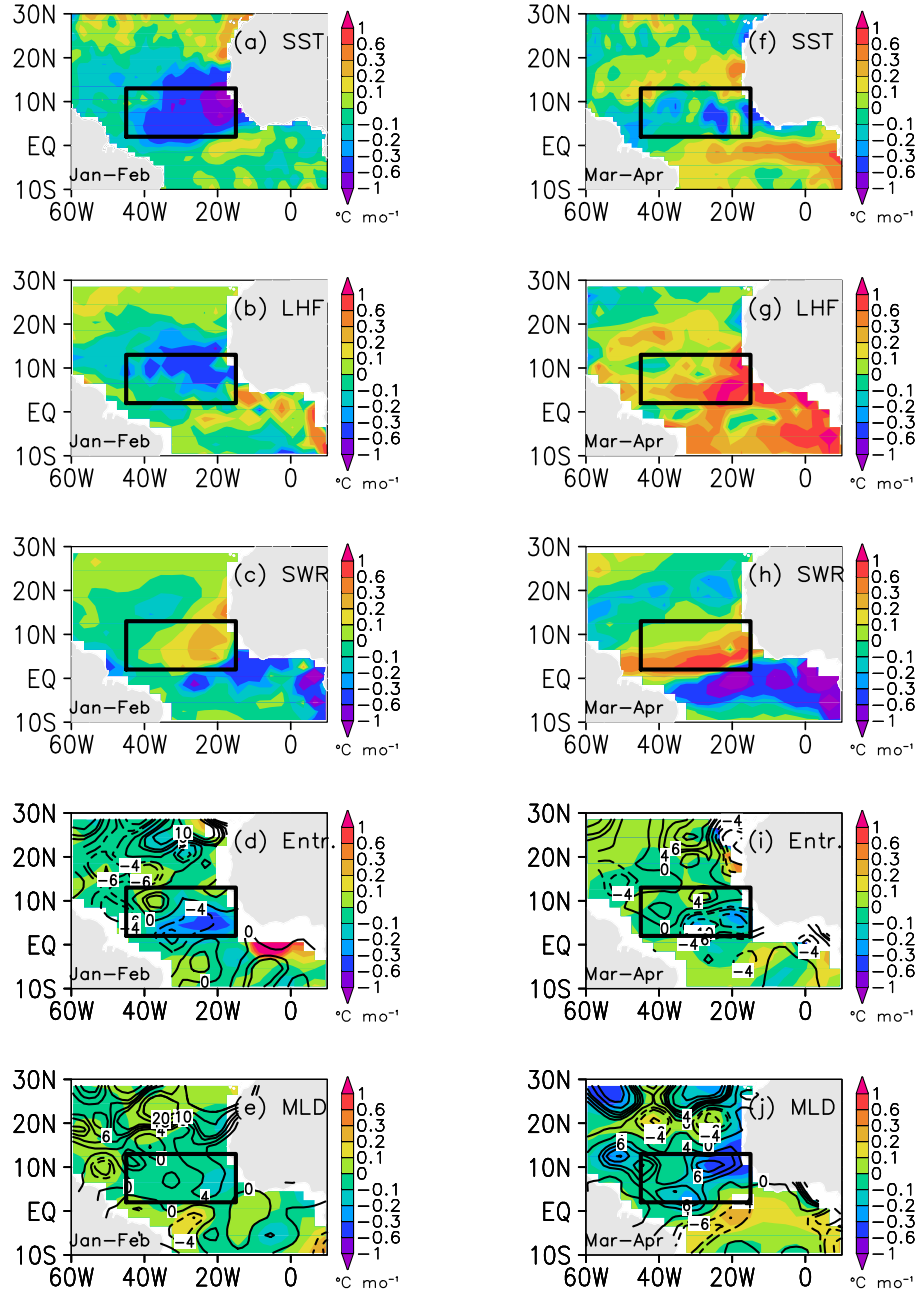
Fig. 5 Terms in the mixed layer temperature budget (eq. 5) averaged during Jan–Feb 2009 (left column) and Mar–Apr 2009 (right column). Negative values indicate anomalous cooling of SST. (a) and (f) Rate of change of SST. (b) and (g) Latent heat flux. (c) and (h) Surface shortwave radiation. (d) and (i) Entrainment, with contours shown for anomalies of 20°C isotherm depth (positive values for deeper than normal and negative values for shallower than normal). (e) and (j) Mixed layer depth (MLD) anomalies acting on the mean surface heat flux, with contours shown for MLD anomalies (positive for deeper than normal and negative for shallower than normal).
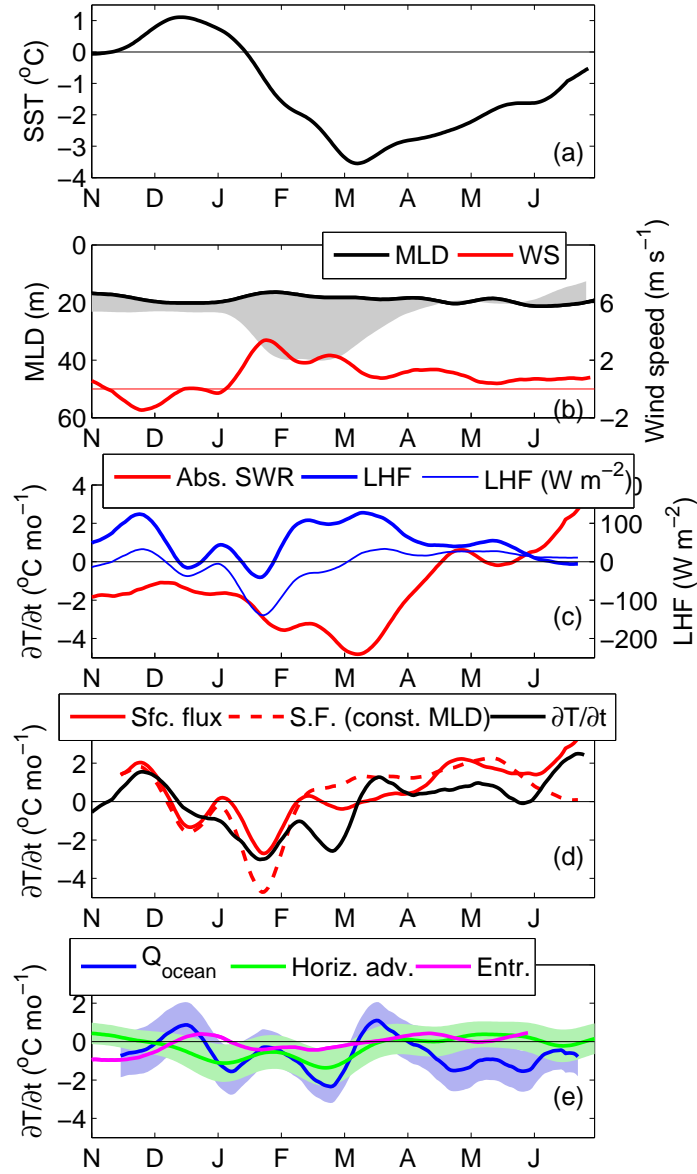
Fig. 6 Measurements from the PIRATA mooring at 12°N, 23°W during Nov 2008 – Jun 2009 (position of mooring is shown in Fig. 2). (a) SST anomaly. (b) Mixed layer depth (MLD) climatology (black) and 2008–09 anomaly (shading), and wind speed anomaly (red). (c) Anomalous contributions from surface latent heat flux (blue) and shortwave radiation absorbed in the mixed layer (red) to changes in SST. Thin blue line is the surface latent heat flux. (d) Anomalies of net surface heat flux (solid red), surface heat flux with MLD held constant (dashed red), and mixed layer temperature rate of change (black). (e) Anomalies of the sum of ocean processes (estimated from the residual in the temperature balance and shown as solid blue curve), horizontal temperature advection (green), and entrainment (pink). Blue and green shading represents one standard error. Anomalies are with respect to Nov 2007 – Jun 2008. Data have been smoothed with a 20-day low-pass filter.
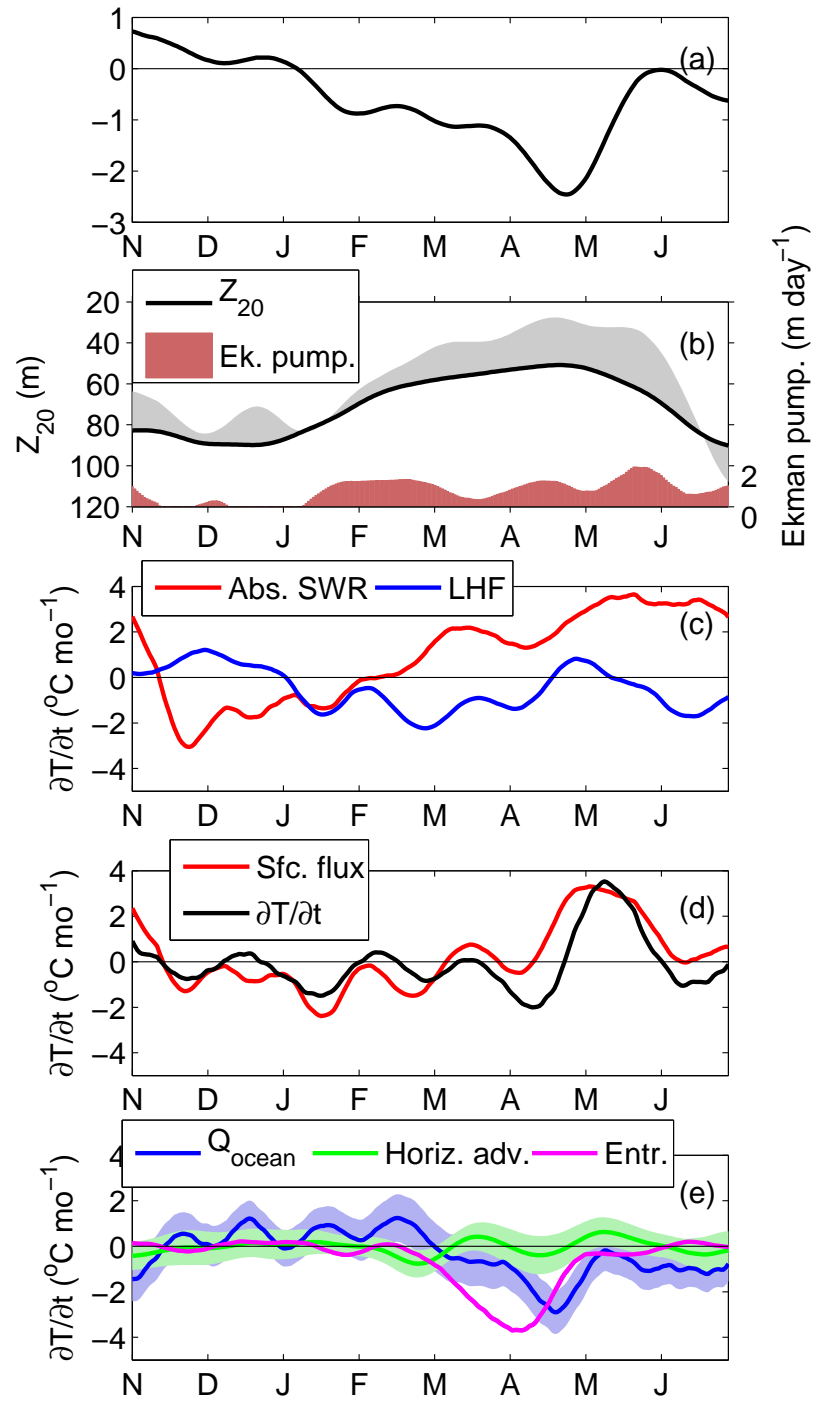
Fig. 7 Same as in Fig. 6 except from the PIRATA mooring at 4°N, 23°W (location shown in Fig. 2) and anomalies are with respect to Nov 2006 – Jun 2007. In (b) the black curve is climatological 20°C isotherm depth (Z_{20}), grey shading is Z_{20} anomaly, and red shading is Ekman pumping anomaly (positive values indicate upwelling).

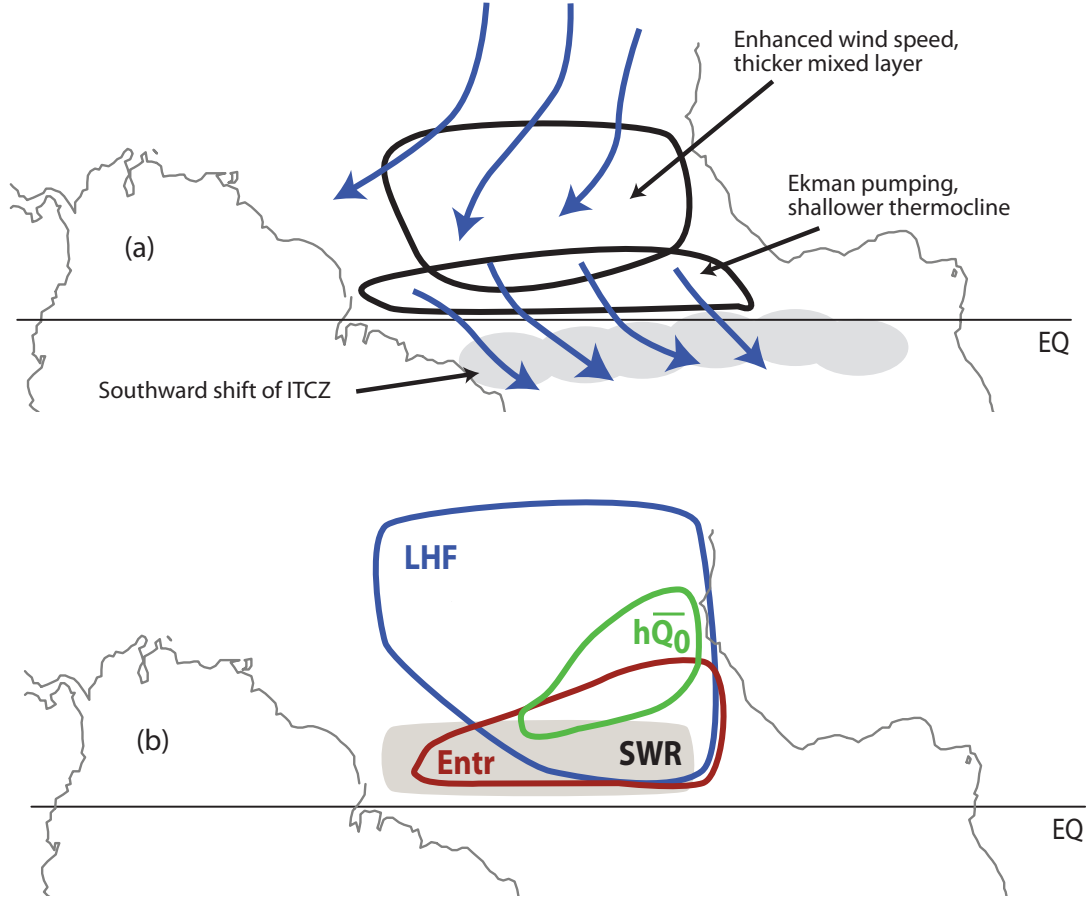**Fig. 8** Schematic diagrams illustrating the processes responsible for generating the SST anomalies during Jan–Apr 2009. Blue arrows in (a) represent anomalies of surface wind velocity. In (b) the blue region is where anomalies of latent heat flux are important, red is entrainment, green is anomalies of mixed layer depth acting on the climatological surface heat flux, and grey shading is surface shortwave radiation.

Table 1 Climatic indices during Dec 2007 – Mar 2008 and Dec 2008 – Mar 2009. All values are monthly anomalies with respect to the corresponding 1982–2009 monthly means, normalized by the standard deviation. Tropical North Atlantic (TNA) wind speed is averaged 15°W–50°W, 5°N–20°N. North Atlantic Oscillation (NAO) index is NCEP/NCAR reanalysis surface pressure at the Azores minus Iceland. The Niño-3.4 index is SST averaged 120°W–170°W, 5°S–5°N. The subtropical high (STH) index is NCEP/NCAR reanalysis surface pressure averaged 30°W–40°W, 20°N–25°N. The Amazon convection index (Amzn) is satellite OLR averaged 30°W–70°W, 10°S–5°N. Negative values of OLR indicate enhanced convection. Bold font for Jan–Feb of each year highlights the months with the strongest positive wind speed anomalies in the TNA in 2009.

	TNA WS	Nino3.4	NAO	STH	Amzn
	2007–08				
Dec	0.2	-1.2	0.5	-0.3	-1.0
Jan	**-0.4**	**-1.4**	**0.4**	**-1.1**	**0.1**
Feb	**0.0**	**-1.8**	**-0.1**	**-0.5**	**-0.3**
Mar	-0.7	-1.4	0.3	-1.2	-1.2
	2008–09				
Dec	-1.0	-0.7	-0.2	-1.2	-0.9
Jan	**2.2**	**-0.7**	**0.9**	**1.5**	**-0.4**
Feb	**1.6**	**-0.7**	**-0.6**	**0.3**	**-0.9**
Mar	-0.2	-0.6	0.1	-1.8	-0.2

Table 2 2009 anomalies of terms in the mixed layer temperature balance, averaged in the ENA region (2°N–12°N, 15°W–45°W) during January–February (left column), March–April (middle), and the total for the January–April period (right column). The first row is the anomalous change in mixed layer temperature due to latent heat flux; second row due to anomalies of absorbed shortwave radiation; third row due to anomalies of mixed layer depth acting on the mean surface heat flux; and fourth row due to entrainment. Fifth row is the sum of the first three rows, and last row is observed (TMI/AMSR-E) anomalous change in SST. Units are °C. Errors for the sum and observed values are one standard error.

901

902

	Jan-Feb	Mar-Apr	Total
LHF	-0.4	0.7	0.3
SWR	0.2	0.5	0.7
MLD	0.0	-0.2	-0.2
Entr	-0.6	-0.1	-0.7
Sum	-0.8±0.5	0.9±0.5	0.1±0.7
Observed	-0.9±0.1	-0.2±0.1	-1.1±0.2